INTERNATIONAL JOURNAL FOR NUMERICAL METHODS IN FLUIDS
Int. J. Numer. Meth. Fluids 2002; **39**:99–120 (DOI: 10.1002/fld.280)

A multi-block lattice Boltzmann method for viscous fluid flows

Dazhi Yu, Renwei Mei and Wei Shyy*,†

Department of Aerospace Engineering, Mechanics & Engineering Science, University of Florida, Gainesville, FL 32611-6250, U.S.A.

SUMMARY

Compared to the Navier–Stokes equation-based approach, the method of lattice Boltzmann Equation (LBE) offers an alternative treatment for fluid dynamics. The LBE method often employs uniform lattices to maintain a compact and efficient computational procedure, which makes it less efficient to perform flow simulations when there is a need for high resolution near the body and/or there is a far-field boundary. To resolve these difficulties, a multi-block method is developed. An accurate, conservative interface treatment between neighboring blocks is adopted, and demonstrated that it satisfies the continuity of mass, momentum, and stresses across the interface. Several test cases are employed to assess accuracy improvement with respect to grid refinement, the impact of the corner singularity, and the Reynolds number scaling. The present multi-block method can substantially improve the accuracy and computational efficiency of the LBE method for viscous flow computations. Copyright © 2002 John Wiley & Sons, Ltd.

KEY WORDS: viscous fluid flow; lattice Boltzmann method; multi-block strategy; grid refinement; corner singularity; Reynolds number scaling

1. BACKGROUND OF THE LATTICE BOLTZMANN METHOD

Recently, there has been much progress in developing the method of the lattice Boltzmann equation (LBE) [1–3] as an alternative, computational technique for solving complex fluid dynamic systems [4, 5]. Adopting a macroscopic method for computational fluid dynamics (CFD), the variables of interest, such as velocity $\boldsymbol{u}$ and pressure p, can be obtained by solving the Navier–Stokes (NS) equations [6–8]. In the LBE approach, one solves the kinetic equation for the particle mass distribution function $f(\boldsymbol{x}, \xi, t)$, and the macroscopic quantities (such as mass density ρ and momentum density $\rho\boldsymbol{u}$) can then be obtained by evaluating the hydrodynamic moments of the distribution function f.

*Correspondence to: Wei Shyy, Department of Aerospace Engineering, Mechanics & Engineering Science, 231 Aerospace Building, University of Florida, Gainesville, FL 32611-6250, U.S.A.
† E-mail: wss@aero.ufl.edu

Received February 2001
Revised October 2001

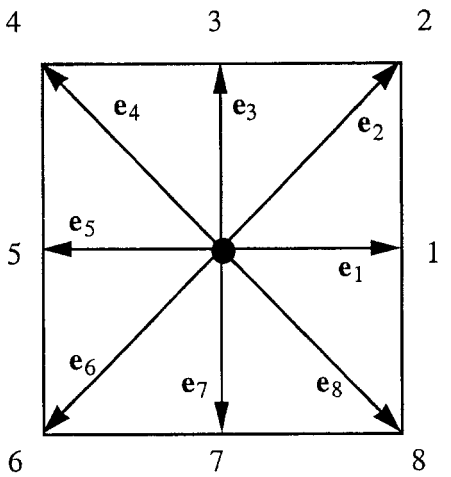

Figure 1. A 2-D, nine-velocity lattice (D2Q9) model.

A popular kinetic model is the Boltzmann equation with the single relaxation time approximation, the so-called BGK model [9]:

$$\frac{\partial f}{\partial t} + \xi \cdot \nabla f = -\frac{1}{\lambda}(f - f^{(eq)}) \tag{1}$$

where ξ is the particle velocity, $f^{(eq)}$ is the equilibrium distribution function (the Maxwell–Boltzmann distribution function), and λ is the relaxation time.

To solve for f numerically, Equation (1) is first discretized in the velocity space using a finite set of velocities $\{\xi_\alpha\}$ without affecting the conservation laws [5, 9–11],

$$\frac{\partial f_\alpha}{\partial t} + \xi_\alpha \cdot \nabla f_\alpha = -\frac{1}{\lambda}(f_\alpha - f_\alpha^{(eq)}) \tag{2}$$

In the above equation, $f_\alpha(\boldsymbol{x}, t) \equiv f(\boldsymbol{x}, \xi_\alpha, t)$ is the distribution function associated with the αth discrete velocity ξ_α and $f_\alpha^{(eq)}$ is the corresponding equilibrium distribution function. The nine-bit square lattice model, which is often referred to as the D2Q9 model (Figure 1) has been successfully used for simulating 2-D flows. For the D2Q9 model, we use $\boldsymbol{e}_\alpha$ to denote the discrete velocity set and we have

$$\begin{aligned} &\boldsymbol{e}_0 = 0, \\ &\boldsymbol{e}_\alpha = c(\cos((\alpha-1)\pi/4), \sin((\alpha-1)\pi/4)) \quad \text{for } \alpha = 1,3,5,7 \\ &\boldsymbol{e}_\alpha = \sqrt{2}c(\cos((\alpha-1)\pi/4, \sin((\alpha-1)\pi/4)) \quad \text{for } \alpha = 2,4,6,8 \end{aligned} \tag{3}$$

where $c = \delta x/\delta t$, δx and δt are the lattice spacing and the time step size, respectively. The equilibrium distribution for the D2Q9 model is in the form of

$$f_\alpha^{(eq)} = \rho w_\alpha \left[1 + \frac{3}{c^2}\boldsymbol{e}_\alpha \cdot \boldsymbol{u} + \frac{9}{2c^4}(\boldsymbol{e}_\alpha \cdot \boldsymbol{u})^2 - \frac{3}{2c^2}\boldsymbol{u} \cdot \boldsymbol{u}\right] \tag{4}$$

where w_α is the weighting factor given by

$$w_\alpha = \begin{cases} 4/9, & \alpha = 0 \\ 1/9, & \alpha = 1,3,5,7 \\ 1/36, & \alpha = 2,4,6,8 \end{cases} \tag{5}$$

With the discretized velocity space, the density and momentum fluxes can be evaluated as

$$\rho = \sum_{k=0}^{8} f_\alpha = \sum_{k=0}^{8} f_\alpha^{(eq)} \tag{6a}$$

and

$$\rho \mathbf{u} = \sum_{k=1}^{8} e_\alpha f_\alpha = \sum_{k=1}^{8} e_\alpha f_\alpha^{(eq)} \tag{6b}$$

The speed of sound in this model is $c_s = c/\sqrt{3}$ and the equation of state is that of an ideal gas,

$$p = \rho c_s^2 \tag{7}$$

Equation (2) can be further discretized in space and time. The completely discretized form of Equation (1), with the time step δt and space step $\boldsymbol{e}_\alpha \delta t$, is:

$$f_\alpha(\boldsymbol{x}_i + \boldsymbol{e}_\alpha \delta t, t + \delta t) - f_\alpha(\boldsymbol{x}_i, t) = -\frac{1}{\tau}[f_\alpha(\boldsymbol{x}_i, t) - f_\alpha^{(eq)}(\boldsymbol{x}_i, t)] \tag{8}$$

where $\tau = \lambda/\delta t$, and $\boldsymbol{x}_i$ is a point in the discretized physical space. The above equation is the discrete lattice Boltzmann equation [1–3] with BGK approximation [9]. The viscosity in the NS equation derived from Equation (8) is

$$v = (\tau - 1/2) c_s^2 \delta t \tag{9}$$

This choice for the viscosity makes formally the LBGK scheme a second order method for solving incompressible flows [10, 11]. The positivity of the viscosity requires that $\tau > 1/2$. Equation (8) can be computed by the following sequence:

$$\text{(i) collision step: } \tilde{f}_\alpha(\boldsymbol{x}_i, t + \delta t) = f_\alpha(\boldsymbol{x}_i, t) - \frac{1}{\tau}[f_\alpha(\boldsymbol{x}_i, t) - f_\alpha^{(eq)}(\boldsymbol{x}_i, t)] \tag{10a}$$

$$\text{(ii) streaming step: } f_\alpha(\boldsymbol{x}_i + \boldsymbol{e}_\alpha \delta t, t + \delta t) = \tilde{f}_\alpha(\boldsymbol{x}_i, t + \delta t) \tag{10b}$$

where $\sim$ denotes the post-collision state of the distribution function. It is noted that on the left-hand-side (LHS) of Equation (10a) and the right-hand-side (RHS) of the Equation (10b) the time level is $t + \delta t$. This is different from the notation for the post-collision state used previously in Reference [12]. In any single-block computation, the specific identification of the time level for the post-collision state is not important since the completion of an LBE computational step is at the end of the streaming step. In the present multi-block computation, the transfer of information between neighboring blocks requires an accurate match in the time

level. Since the post-collision state variables are obtained after a physical relaxation process, it is appropriate to associate the time $t + \delta t$ to the variables of this state. Such a change in the notation does not affect the derivation for the post-collision value $\tilde{f}_\alpha(\boldsymbol{x}_i, t + \delta t)$ given in Reference [12]. It is noted that the collision step is completely local and the streaming step takes very little computational effort. Equation (10) is explicit, easy to implement, and straightforward to parallelize.

Those inherent advantages of the LBE method necessitate the use of a regular lattice structure (such as a square lattice or hexagonal lattice) with uniform spacing. This is in direct contrast to the many finite difference/volume/element methods in which body-fitted coordinates are used and the grid stretching can be easily applied. However, it should be noted that there has also been a growing interest in the macroscopic method to employ the Cartesian grid for complex flow problems [13, 14]. A challenge of the uniform grid is to offer high resolution near a solid body and to place the outer boundary far away from the body without wasting the grid resolution elsewhere. In order to use the regularly spaced lattice while developing the capability to place the outer boundary far away, it is desirable to divide the computational domain into a number of grid blocks so that within each block uniform lattice spacing can be used. Again, such a multi-block approach has been actively employed in the Navier–Stokes equation methods with both Cartesian and curvilinear coordinates.

This paper describes a multi-block strategy for the LBE method. In each block, constant value of $\delta x = \delta y = \delta t$ is used. The information exchange on the interface between the neighboring blocks of different lattice spacing δx for the primary variables f_α's is implemented to ensure the mass conservation and the continuity of stresses between blocks.

Several studies addressing the multi-block techniques have recently appeared in the literature. In particular, Reference [15] first reports an approach with which the present study shares a common concept. However, as will be presented later, details of the approaches employed in Reference [15] and in this study are different. In Reference [15], values of the distribution functions on the coarse grid, transmitted from regions of finer patches, including gradients of hydrodynamic variables, are calculated with second-order interpolation in space and time in the boundary nodes of the fine grid. A more accurate approach will be proposed along with a detailed computational procedure to enable the research community to consider the entire approach with adequate details.

After the completion of the present work, two papers were published: References [16, 17]. In Reference [16], the coarse base grid covers the entire physical domain, and the finer grid blocks are placed at regions where local grid refinement is desirable. The simulation is first carried out on the base grid level at a smaller relaxation time, allowing a rapid propagation of boundary information throughout the entire domain. At a later time, the computation of the fine grid variables is initiated. The dependent variables on both grid levels are, then, advanced in time simultaneously with the fine grid boundary conditions obtained from the base grid solution at the grid interface. Reference [17] is based on multiple nested lattices with increasing resolution. The discrete velocity Boltzmann equation is solved numerically on each sub-lattice and interpolation between the interfaces is carried out in order to couple the computations in different blocks. Compared to the above-cited references, in the present method, the different grid size blocks are not overlapped between each other, and blocks are connected only through the interface.

In the present effort, the conservative properties and block-to-block coupling are directly investigated. Furthermore, a systematic effort has been made to both accuracy and efficiency aspects. Several test cases have been employed. A lid-driven cavity flow is computed using a single block with uniform grid and the present multi-block method. The results are compared with published benchmark results. A channel flow with a parabolic velocity profile at the inlet over an asymmetrically placed cylinder at $Re = 100$ (based on the average incoming velocity) is computed next using the multi-block method. Finally, flow over NACA0012 airfoil at $Re = 500$–5000 is computed. The present study demonstrates that the multi-block strategy can greatly improve the computational efficiency of the LBE method. Important computational issues, such as conservative properties between grid blocks, accuracy assessment with respect to grid refinement, the presence of the corner singularity, and the implications of the Reynolds number, have not been adequately addressed in the literature, and will be presented in this work.

2. BASICS OF THE MULTI-BLOCK STRATEGY IN THE LBE METHOD

To illustrate the basic idea, a two-block system (a coarse and a fine, as shown in Figure 2(a)) is considered in the derivation for the interfacial information exchange. The ratio of the lattice space between the two-grid system is

$$m = \delta x_c / \delta x_f \tag{11}$$

For a given lattice size δx, the viscosity of the fluid is

$$v = (2\tau - 1)\delta_x c/6 \tag{12}$$

In order to keep a consistent viscosity, and thus Re, in the entire flow field involving different lattice sizes, the relation between relaxation times, τ_f, on the fine grid, and τ_c, on the coarse gird, must obey the following rule:

$$\tau_f = \frac{1}{2} + m\left(\tau_c - \frac{1}{2}\right) \tag{13}$$

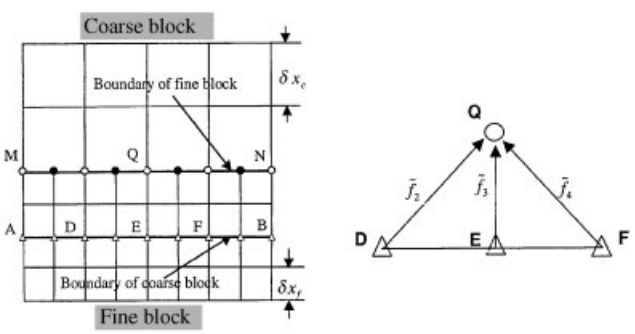

Figure 2. (a) Interface structure between two blocks of different lattice spacing. (b) Flow chart of the computational procedure in the present multi-block method.

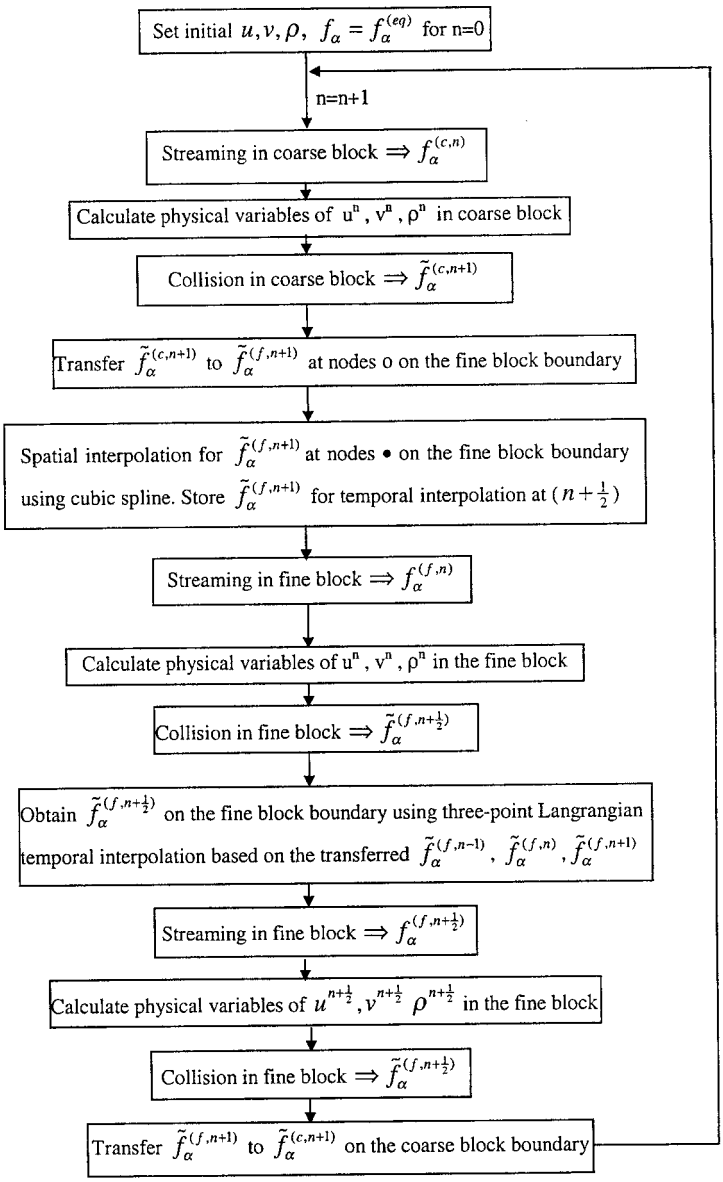

Figure 2. *Continued.*

for $c = 1$. To keep the variables and their derivatives continuous across an interface between two different grids, a consistent and accurate relationship for the probability density function in the neighboring grid blocks must be developed. The following summarizes the key elements in the derivation for the information exchange across the interface.

It is noted that,

$$f_\alpha(\boldsymbol{x},t) = f_\alpha^{(eq)}(\boldsymbol{x},t) + f_\alpha^{(neq)}(\boldsymbol{x},t) \tag{14}$$

where $f^{(neq)}$ is the non-equilibrium part of the distribution function based on which the deviatoric stresses are evaluated. The collision step (Equation (10a)) gives

$$\tilde{f_\alpha}(\boldsymbol{x}_i, t+\delta t) = \left(1 - \frac{1}{\tau}\right) f_\alpha(\boldsymbol{x}_i, t) + \frac{1}{\tau} f_\alpha^{(eq)}(\boldsymbol{x}_i, t) \tag{15}$$

Substituting Equation (14) into Equation (15) leads to

$$\begin{aligned}\tilde{f_\alpha}(\boldsymbol{x}_i, t+\delta t) &= \left(1 - \frac{1}{\tau}\right)[f_\alpha^{(eq)}(\boldsymbol{x}_i, t) + f_\alpha^{(neq)}(\boldsymbol{x}_i, t)] + \frac{1}{\tau} f_\alpha^{(eq)}(\boldsymbol{x}_i, t) \\ &= f_\alpha^{(eq)}(\boldsymbol{x}_i, t) + \frac{\tau - 1}{\tau} f_\alpha^{(neq)}(\boldsymbol{x}_i, t)\end{aligned} \tag{16}$$

Denoting the coarse-grid quantities with the superscript c and fine-grid quantities with the superscript f, the post-collision step gives

$$\tilde{f}_\alpha^{(c)} = f_\alpha^{(eq,c)} + \frac{\tau_c - 1}{\tau_c} f_\alpha^{(neq,c)} \tag{17}$$

Similarly,

$$\tilde{f}_\alpha^{(f)} = f_\alpha^{(eq,f)} + \frac{\tau_f - 1}{\tau_f} f_\alpha^{(neq,f)} \tag{18}$$

Since the velocity and density must be continuous across the interface between the two grids, from Equation (4), it is seen that

$$f_\alpha^{(eq,c)} = f_\alpha^{(eq,f)} \tag{19}$$

To maintain continuity in deviatoric stresses, in the 2-D case,

$$\tau_{ij} = \left(1 - \frac{1}{2\tau}\right) \sum_{\alpha=1}^{8} f_\alpha^{(neq)}(\boldsymbol{e}_{\alpha i}\boldsymbol{e}_{\alpha j} - \tfrac{1}{2}\, e_\alpha \cdot e_\alpha \delta_{ij}) \tag{20}$$

it is obvious that one requires

$$\left(1 - \frac{1}{2\tau_c}\right) f_\alpha^{(neq,c)} = \left(1 - \frac{1}{2\tau_f}\right) f_\alpha^{(neq,f)} \tag{21}$$

or

$$f_\alpha^{(neq,c)} = m \frac{\tau_c}{\tau_f} f_\alpha^{(neq,f)} \tag{22}$$

Substituting Equation (22) into Equation (17) one obtains

$$\tilde{f}_\alpha^{(c)} = f_\alpha^{(eq,c)} + m\, \frac{\tau_c - 1}{\tau_f} f_\alpha^{(neq,f)} \tag{23}$$

Using Equations (18) and (19), the above becomes

$$\tilde{f}_\alpha^{(c)} = f_\alpha^{(eq,f)} + m\,\frac{\tau_c - 1}{\tau_f}\,\frac{\tau_f}{\tau_f - 1}[\tilde{f}_\alpha^{(f)} - f_\alpha^{(eq,f)}] = f_\alpha^{(eq,f)} + m\,\frac{\tau_c - 1}{\tau_f - 1}[\tilde{f}_\alpha^{(f)} - f_\alpha^{(eq,f)}] \tag{24}$$

In transferring the data from the coarse grids to the fine grids, one similarly obtains

$$\tilde{f}_\alpha^{(f)} = f_\alpha^{(eq,c)} + \frac{\tau_f - 1}{m(\tau_c - 1)}[\tilde{f}_\alpha^{(c)} - f_\alpha^{(eq,c)}] \tag{25}$$

Equations (24) and (25) were first given in Reference [15]. On the interface between two blocks, there are m values of $\tilde{f}_\alpha^{(f)}$ needed for each $f_\alpha^{(eq,c)}$ and $\tilde{f}_\alpha^{(c)}$. Thus, spatial and temporal interpolation procedures for the values of $\tilde{f}_\alpha^{(eq,c)}$ and $\tilde{f}_\alpha^{(c)}$ on the fine-grid lattice are used to complete the evaluation of $\tilde{f}_\alpha^{(f)}$.

3. THE INTERFACE STRUCTURE AND COMPUTATIONAL PROCEDURE

The typical interface structure is shown in Figure 2(a). The line $\overline{\mathrm{MN}}$ is the fine block boundary, while the line $\overline{\mathrm{AB}}$ is the coarse block boundary. The coarse block boundary is in the interior of the fine block, and the fine block boundary is in the interior of the coarse block. This arrangement of the interface is convenient for the information exchange between two neighboring blocks. For example, grid Q is an interior lattice node of the coarse block. After the collision step, the values of incoming distribution functions $\tilde{f}_2(t^{n+1}, X_D)$, $\tilde{f}_3(t^{n+1}, X_E)$ and $\tilde{f}_4(t^{n+1}, X_F)$ from boundary nodes D, E, and F, respectively, are needed in order to obtain $f_2(t^{n+1}, X_Q)$, $f_3(t^{n+1}, X_Q)$, and $f_4(t^{n+1}, X_Q)$ at the end of steaming step, since other components of $f_\alpha(t^{n+1}, X_Q), (\alpha = 1, 5, 6, 7, 8)$ are obtained from advecting the neighboring post-collision values of $\tilde{f}_\alpha$ in the interior nodes of the coarse block. For the same reason, the fine block boundary $\overline{\mathrm{MN}}$ is located in the interior of the coarse block. However, on the fine block boundary $\overline{\mathrm{MN}}$, there is no information on the nodes denoted by the solid symbol • in Figure 2(a); it must be obtained through spatial interpolation based on the information at the nodes denoted by the open symbol ∘ on the line $\overline{\mathrm{MN}}$. To eliminate the possibility of spatial asymmetry caused by interpolations, a symmetric, cubic spline fitting is used for spatial interpolation of $\tilde{f}_\alpha$ on the fine block boundary,

$$\tilde{f}(x) = a_i + b_i x + c_i x^2 + d_i x^3, \quad x_{i-1} \leqslant x \leqslant x_i, \ i = 1, \ldots, n \tag{26}$$

where the constants (a_i, b_i, c_i, d_i) are determined by using the continuity of the nodal conditions of f, f', f'' and suitable end conditions (such as zero second derivative for f). We found that it is very important to maintain the spatial symmetry in the interpolation along the interface.

Figure 2(b) shows the flow chart of the computational procedure for the multi-block calculation. It is noted that in addition to the spatial interpolation, there is a need for temporal interpolation on all nodes at the fine block boundary $\overline{\mathrm{MN}}$ in order to obtain $\tilde{f}_\alpha(t^{n+1/2}, \overline{\mathrm{MN}})$. Here a three-point Lagrangian formula is used.

$$y(t) = \sum_{k=1}^{3} y_k \left(\prod_{\substack{j=1 \\ j \neq k}} \frac{t - t_i}{t_k - t_j} \right) \tag{27}$$

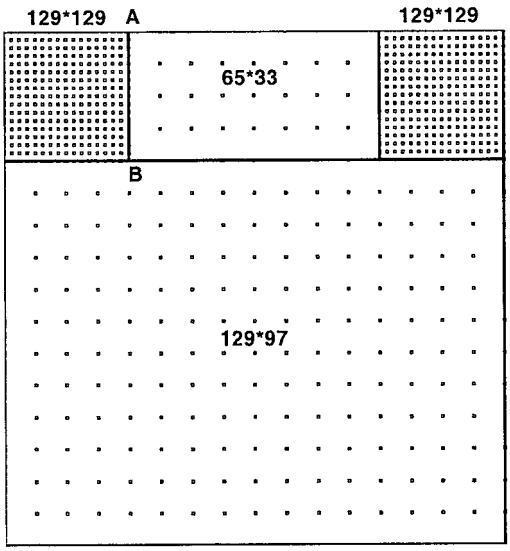

Figure 3. Block layout for a 2-D cavity. Lattice spacing is reduced by a factor of 8 for graphical clarity.

4. RESULTS AND DISCUSSIONS

Several well-documented flow problems are selected to highlight the performance of the present method. In all cases, the boundary condition for f_α in the solid region near a wall is obtained using the formulations given in Reference [12] for a curved geometry.

4.1. Lid-driven cavity flow

The lid-drive cavity flow has been extensively used as a benchmark solution to test the accuracy of a numerical method. In this flow, two singular points at the upper corners of the lid require high resolution to obtain satisfactory stress distribution near the corner points. To assess the LBE results, the benchmark solutions of Reference [18] are used for comparison.

The computations are carried out using (i) a single-block with uniform lattice (129×129) with the walls placed halfway between lattices, and (ii) a multi-block whose layout is shown in Figure 3. For the multi-block case, in the two upper corner regions, the grid resolution is increased by a factor of 4. For $Re = 100$, the relaxation time is $\tau_c = 0.56$ for the coarse-grid block and $\tau_f = 0.74$ for the fine-grid block. The upper wall velocity is $U = 0.0156$. The initial condition for density is unity and that for velocity is zero. The streamlines shown in Figure 4 are obtained from the single block solution and the pattern is not discernable from those of the multi-block solution. The positions of the centers of the primary vortices are (0.6154, 0.7391) and (0.6172, 0.7390) for uniform grid and multi-block solutions respectively, compared well with the value (0.6172, 0.7344) from Reference [18]. The u- and v-components of the velocity along the vertical line and horizontal line through the geometry center are shown in Figure 5(a) and (b), respectively. It is seen that while the single block method with 129×129 lattices can capture most of the physical variables satisfactorily, the multi-block method can improve the numerical accuracy. Figure 6 shows the pressure contour from the

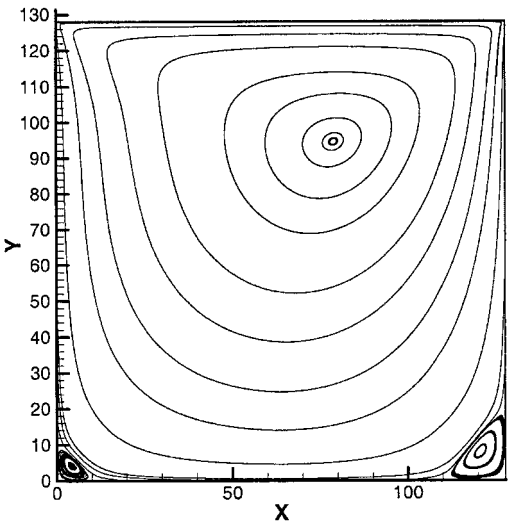

Figure 4. Streamlines in the cavity flow at $Re = 100$.

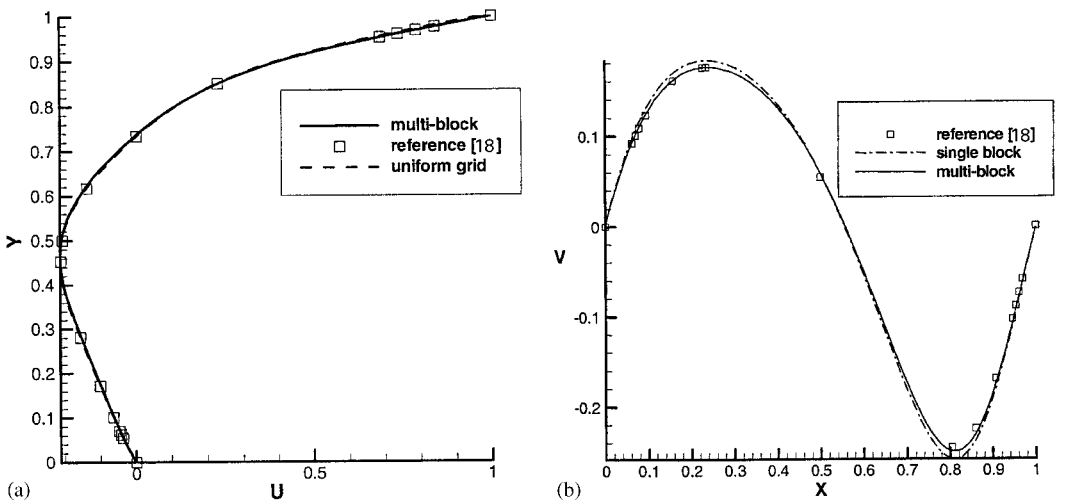

Figure 5. (a) Comparison of u-velocity along the vertical line through geometric center. (b) Comparison of velocity between present results and those in Reference [18].

single-block computation. Because of the singularity at the upper corners, the density contours exhibit noticeable oscillations due to the insufficient resolution near singularities. Figure 7 shows the pressure contours obtained from the multi-block solution. Significant improvement in the smoothness of the solution for the pressure field over that of the single block solution is observed.

In an NS solver for incompressible flows, because of the decoupling of thermodynamic pressure and velocity field, it is crucial to maintain the mass conservation of the entire flow

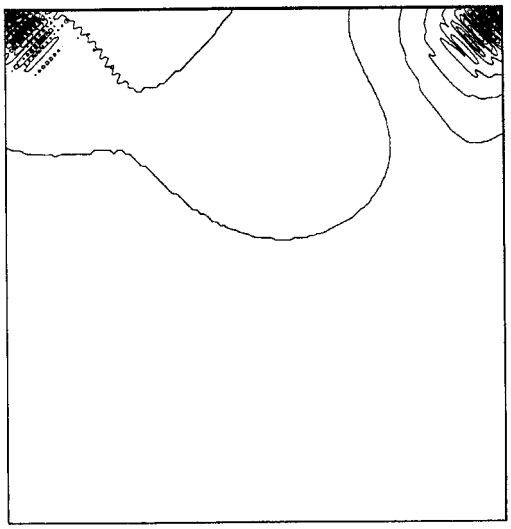

Figure 6. Pressure contours in the cavity flow from the single-block LBE simulation.

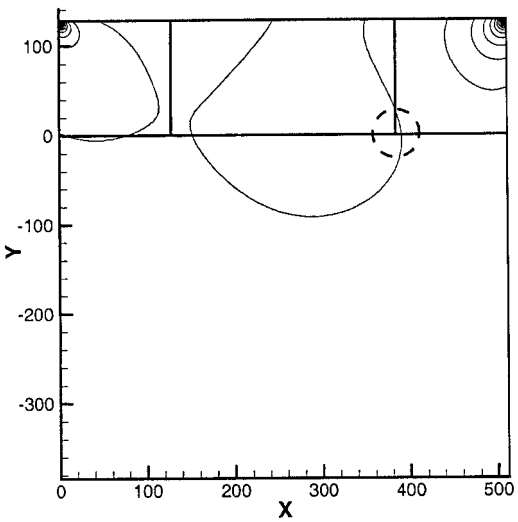

Figure 7. Pressure contours in the cavity from multi-block LBE solution. (For the circled region, see Figure 8).

domain. This issue becomes more critical when the multi-block method is used [8, 19]. Also for incompressible flows, the pressure is arbitrary up to a constant. Hence coupling the pressure term while maintaining the mass flux conservation is very important. Generally speaking, it is difficult to maintain simultaneously the continuity of mass, momentum, and stresses across the interface between neighboring blocks because interpolations are applied to each

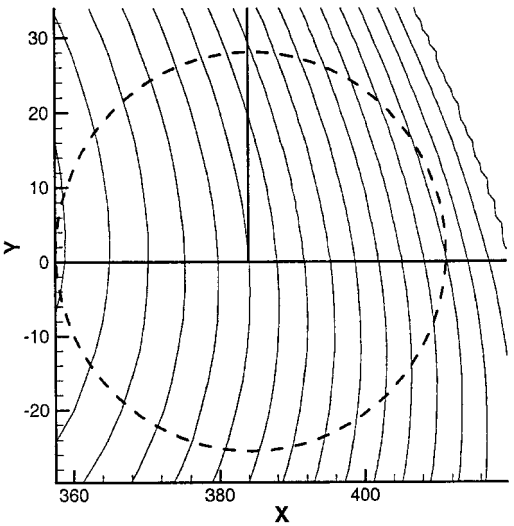

Figure 8. Enlarged view of pressure contour in the circled region in Figure 7 near the intersection of three blocks. The figure demonstrates that the block interface and corner and well handled.

dependent variable. In the present multi-block LBE method, the continuities of mass and stresses are ensured through the use of Equations (24) and (25). The most important point is that interpolations are only applied to f_i's along the interface and this automatically ensures the consistency in the transfer of various flux terms across the interface.

To validate the above arguments, pressure, shear stress, mass flux and momentum flux near the block interfaces are examined next. Figure 8 shows a local, enlarged view of the pressure contour around an interface corner point indicated by the circle in Figure 7. Clearly, the pressure is rather smooth across the interface with the coarse-to-fine grid size ratio of $m = 4$. Figures 9–11 show the contours of shear stress, mass flux, and momentum flux ρu_x^2. It is seen that these physical quantities are all smooth across the interface.

To demonstrate this issue more clearly, macroscopic physical quantities on one part of the interface (i.e. line A–B in Figure 3) are plotted in Figures 12–17. After the streaming step there is no physical value on the interface for the fine grid. Here we use a second order extrapolation to obtain the fine grid value on the interface. Figures 12–15 show that mass and momentum fluxes match very well between the fine- and coarse-grid. Figure 16 shows the shear stress profile. In most parts of the interface the fine- and coarse-grid solutions agree very well with each other. The discrepancy appears near the upper wall. It is noted that in the fine-grid blocks, the top moving wall is located half-way between two horizontal, fine-grid lattices with a distance of $\Delta_f \delta x_f = 0.5\delta x_f$. In the coarse-grid block, the distance between the wall to the nearest lattice in the fluid region is $\Delta_c \delta x_c = 0.5\delta x_f = 0.5\delta x_c/4 = 0.125\delta x_c$ for $m = 4$. This mismatch ($\Delta_f \neq \Delta_c$) will result in different truncation errors in the boundary condition for f_i's. This subsequently affects the accuracy of the shear stress near the corner of the block interface and the wall. The same problem also appears in Figure 17 for pressure. The behavior of the solution, however, can be easily improved by using a set of uniform-sized fine grids for the fluid region near the entire upper wall.

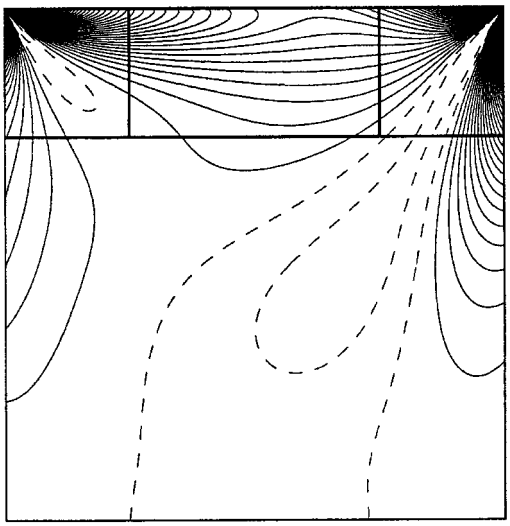

Figure 9. Shear stress contour. Solid and dash lines represent positive and negative values, respectively.

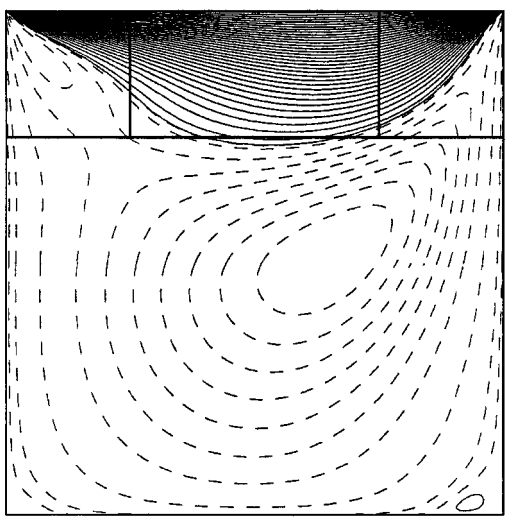

Figure 10. Contour of x-component mass flux ρu_x. Solid and dash lines represent positive and negative values, respectively.

4.2. Channel flow over an asymmetrical placed cylinder at $Re = 100$

Schäfer and Turek [20] reported a study of a laminar flow over a circular cylinder placed asymmetrically inside a channel. The cylinder center to the upper wall distance is 4.2 cylinder radii, and the cylinder center to the lower wall distance is 4.0 radii. In the present LBE computation, two grid sizes are used with the coarse-to-fine lattice spacing ratio $m = 4$ and

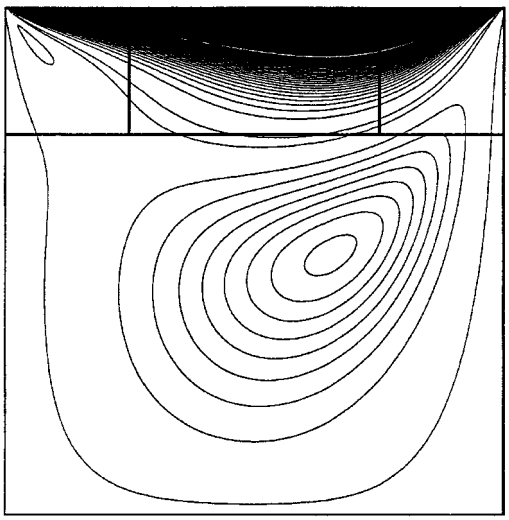

Figure 11. Contour of momentum flux in the x-direction $\rho \cdot u_x^2$.

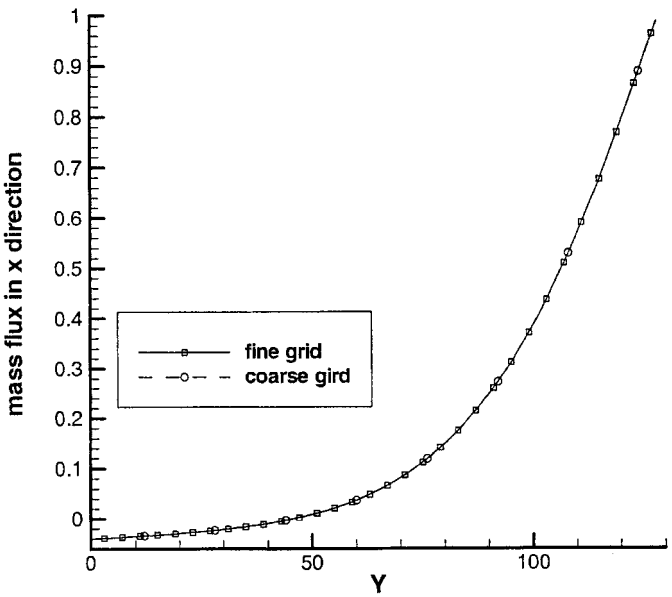

Figure 12. The x-component of the mass flux $\rho u_x/(\rho_0 U)$ on the interface AB defined in Figure 3. In Figures 12–15, $\rho_0 = 1$and $U = 0.0156$.

the flow domain is divided into five blocks. The finer grid block is placed around the cylinder as shown in Figure 18. The radius of the cylinder, r, equals 20 lattice spacing in the fine block. The total number of lattices in coarse-grid blocks is 8854, and the fine block has $81 \times 81 = 6561$ lattices. The relaxation times for the coarse- and fine-grids are $\tau_c = 0.52$

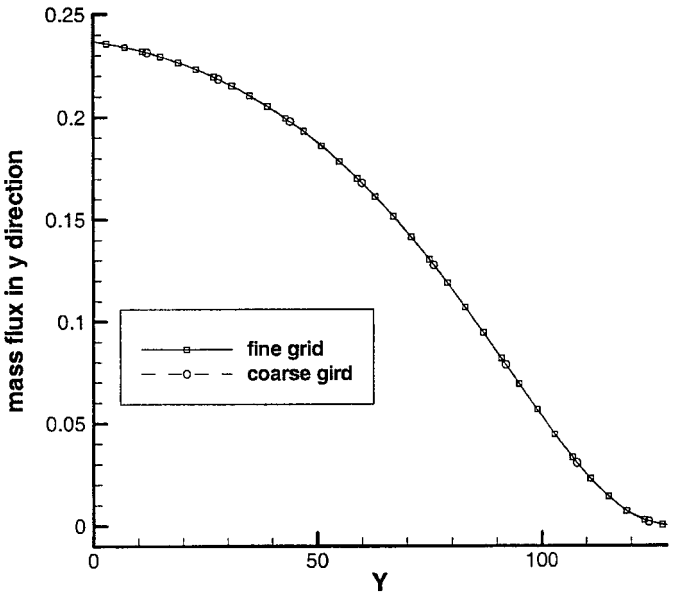

Figure 13. The x-component of the mass flux $\rho u_y/(\rho_0 U)$ on the interface AB.

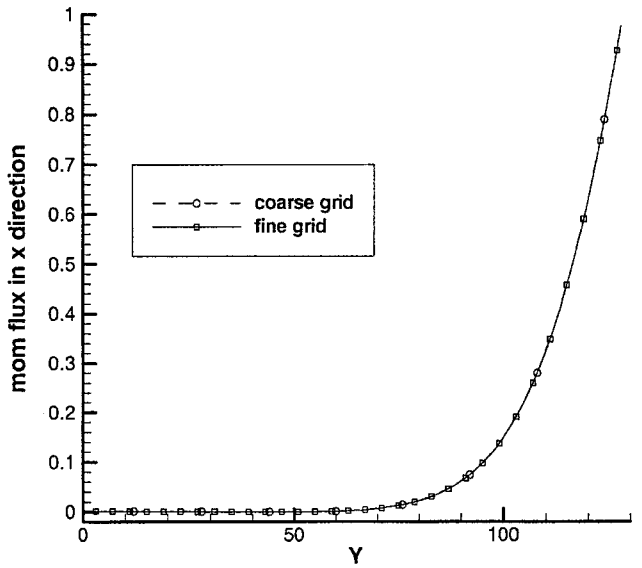

Figure 14. The x-component of the momentum flux $\rho u_x^2/\rho_0 U^2$, on the interface AB.

and $\tau_f = 0.58$, respectively. The average inlet velocity $\bar{U}$ is 0.0666. The channel inlet has a parabolic velocity and is located at 4.0 radii upstream of the cylinder center. A zeroth-order extrapolation for f_α is used at the outlet. The Reynolds number based on the average inlet velocity and the diameter of the cylinder is $Re = 100$.

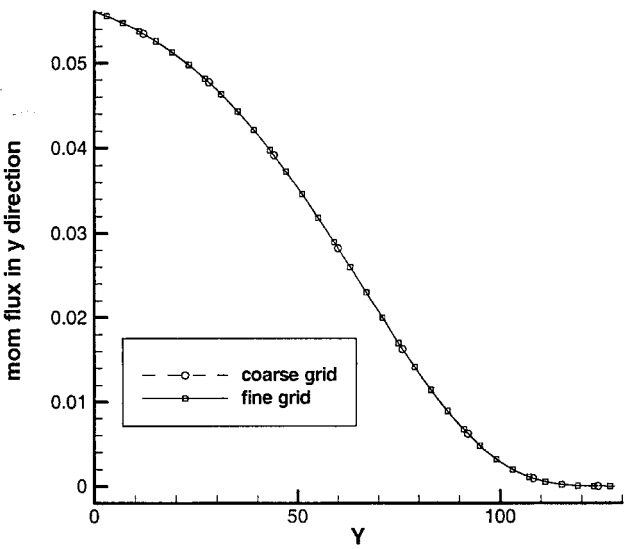

Figure 15. The y-component of the momentum flux $\rho u_x u_y/\rho_0 U^2$, on the interface AB.

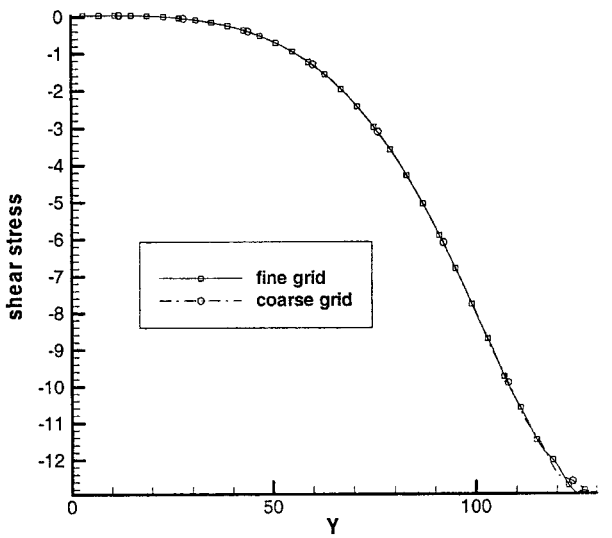

Figure 16. Shear stress $\tau_{xy}/(\mu U/H)$ on the interface AB.

At this Reynolds number, the flow becomes unsteady and periodic vortex shedding is observed. The numerical value of Strouhal number ($St = D/\bar{U}T$) is 0.300 and it agrees very well with the range of values (0.2995–0.305) given in Reference [20]. Here D is the diameter of cylinder and T is the peak-to-peak period of the lift force which is 500 in lattice unit based on the coarse block. An instantaneous streamline plot is shown in Figure 18 after the dynamically periodic solution is established. The variations of the drag and lift coefficients

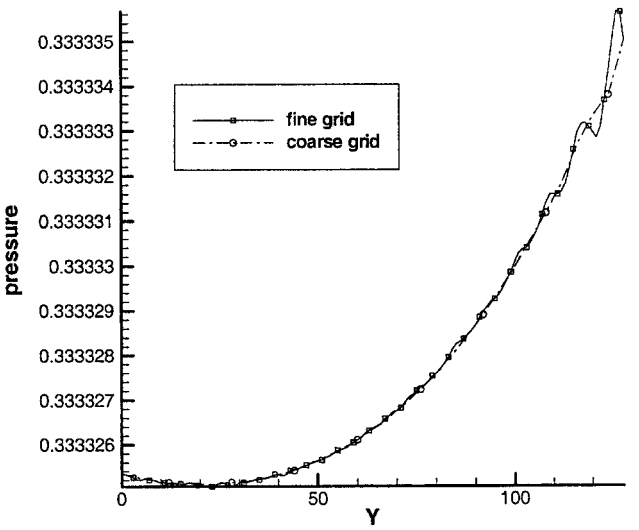

Figure 17. Pressure on the interface AB.

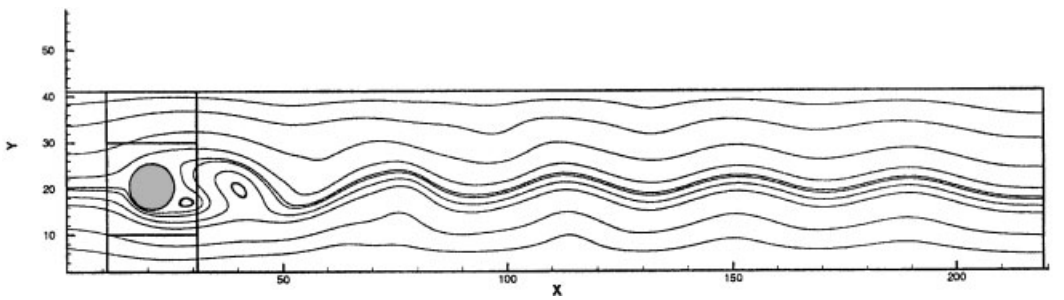

Figure 18. Instantaneous streamlines for channel flow over an asymetrically placed cylinder at $Re = 100$.

are shown in Figure 19. It is noted that $C_D(t)$ has two peaks ($C_{D,\max 1} = 3.23,\ C_{D,\max 2} = 3.22$). A closer examination of $C_L(t)$ reveals that $C_L(t)$ is not symmetric with respect to the x-axis ($C_{L,\max} = 1.01, C_{L,\min} = -1.03$). This result is reasonable because the flow is not symmetric with respect to the horizontal line drawn through the center of the cylinder. The mean velocity of the flow passing the upper region of cylinder is lower than that passing the lower region [20]. Careful examination of the computational flow filed indicates that the local pressure in the upper region is higher than that in the lower region at similar stages of the vortex shedding. There is no report of the existence of two peaks of $C_D(t)$ and asymmetry of $C_L(t)$ in Reference [20]. Only the ranges of $C_{D,\max}$ (3.22–3.24) and $C_{L,\max}$ (0.99–1.01) were given. The present results for $C_{D,\max}$ and $C_{L,\max}$ are well within those ranges.

4.3. Steady flow over NACA0012 airfoil

The NACA0012 airfoil (Figure 20) is a popular wing model that has been used extensively. Flow fields at $Re = 500, 1000, 2000$, and 5000 are computed with the multi-block LBE scheme.

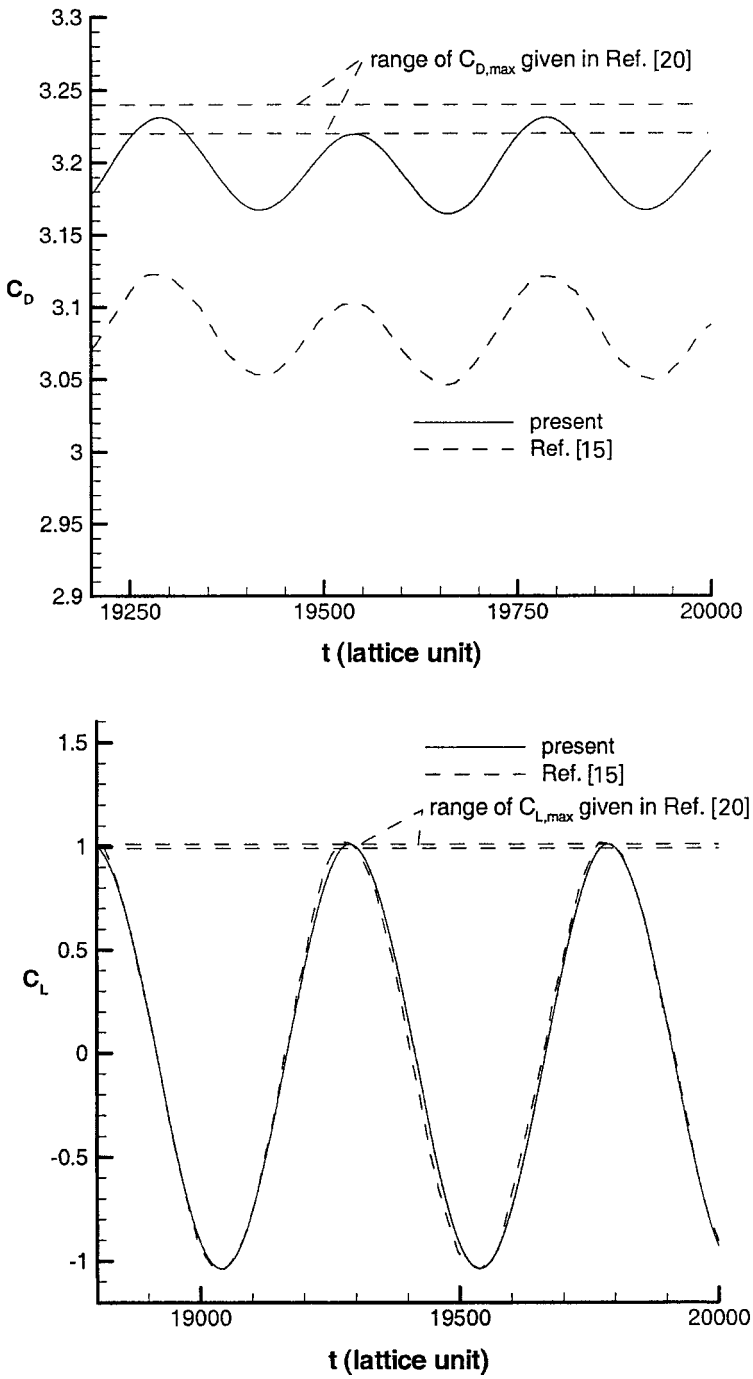

Figure 19. Unsteady drag and lift coefficient on the cylinder.

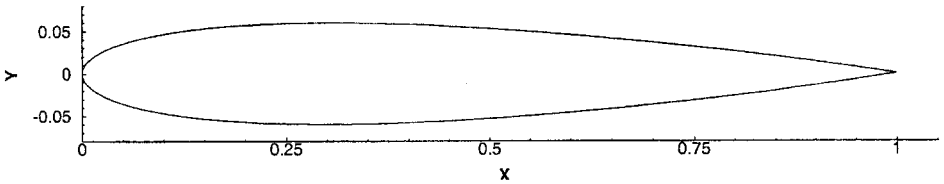

Figure 20. NACA0012 airfoil.

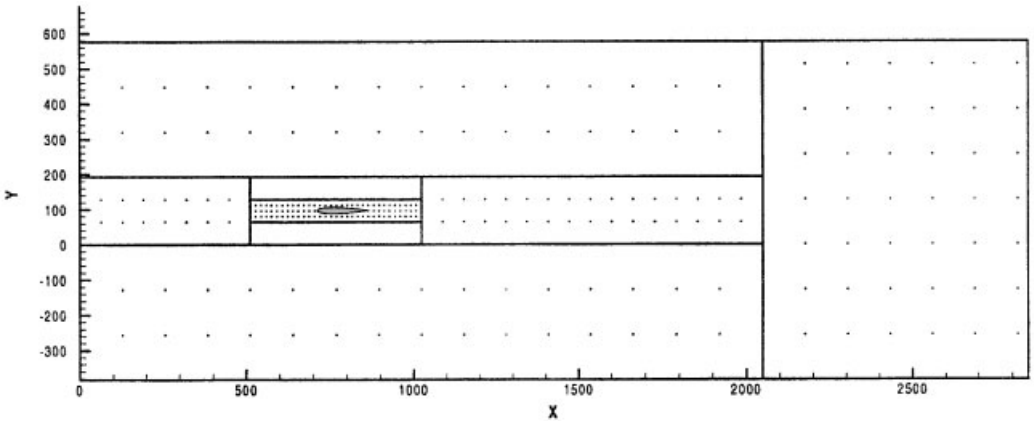

Figure 21. Block and lattice layout for flow over NACA0012. The lattice spacing is reduced by a factor32 for graphical clarity.

Figure 21 shows the entire computational domain and the schematic diagram of the multi-block arrangement. There are 300 lattices (grids) along the chord in the finest block. The largest grid size ratio between neighboring blocks is 4. At the inlet, upper, and lower boundaries, the equilibrium values are used for f_i's according to Equation (4) based on the free-stream velocity. At the downstream boundary a zeroth order extrapolation for f_i's is used.

Figure 22 shows the density contour, streamlines and velocity vector of the converged solution at $Re = 2000$ and zero angle of attack. To investigate the effect of grid resolution, two sets of grid systems are used for the flow field at $Re = 500$: a fine grid system and a coarse grid system (with resolution reduced by a factor of 2 in every block). Figure 23 shows the velocity profiles at $(x - x_{LE})/L = 0.06$ where L is the chord length and x_{LE} is the location of the leading edge. These two sets of velocity profile agree well with each other, although the fine grid solution appears to have smoother u-component velocity profile, as expected.

Figure 24 compares the drag coefficient C_d between the present LBE simulation and those calculated from Xfoil, which is a coupled inviscid and boundary layer flow solver [21]. It can be seen that two sets of results agree with each other very well for the range of Reynolds numbers investigated in this study.

It is also noted that at $Re = 500$, the present value of $C_d = 0.1761$ compare very well with the results reported in Reference [22]: $C_d = 0.1762$ obtained using a Navier–Stokes equation-

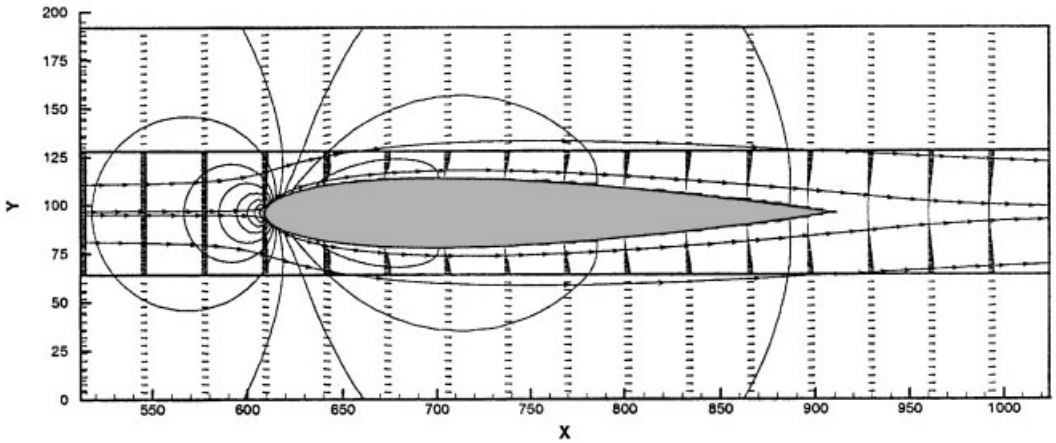

Figure 22. Streamlines, pressure contour, velocity vector for a uniform flow over NACA 0012 airfoilat $Re = 2000$.

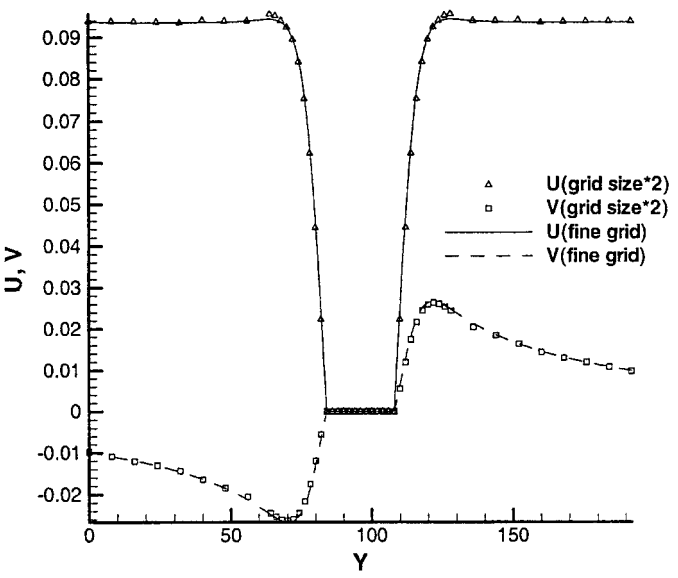

Figure 23. Grid-independence test of the velocity profiles near the leading edge at $(x - x_{LE})/L = 0.06$ for flow over NACA0012 airfoil at $Re = 500$.

based finite difference method, and $C_d = 0.1717$ using Powerflow code developed by EXA Corporation, which is based on the lattice Boltzmann equation method. In addition, the present simulation for the symmetrical flow at $Re = 500$ gives a lift coefficient of $|C_L| < 6 \times 10^{-14}$. Reference [22] reported $C_L = 1.15 \times 10^{-7}$ using an NS equation-solver and $C_L = 2.27 \times 10^{-4}$ using EXA's Powerflow code. This suggests that the present multi-block code preserve the symmetry very well.

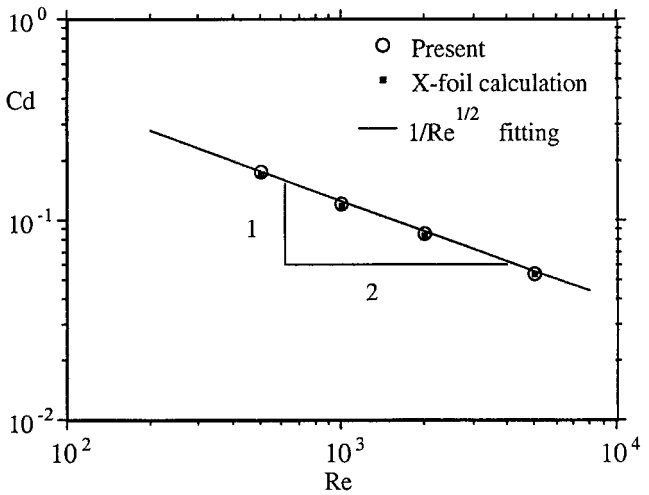

Figure 24. Comparison of C_d between the present simulation and Xfoil calculation as a function of Re for flow over NACA0012 airfoil. The straight line is the slope according to the laminar boundary layer theory.

It is worth pointing out that there is a significant saving in the computational cost using the multi-block method in LBE simulations. There are three different sizes of grids used for the NACA0012 airfoil simulation. There are $1025 \times 129 = 132\,225$ fine grids, 93 200 intermediate grids with $m = 4$, and 139 628 coarse grids (with $m = 8$ in reference to the finest grids). This gives a total of about 3.6×10^5 grids in the entire domain. If the fine grid system is used in the entire domain, the number of the grids would be $N_x \times N_y = 5698 \times 1153 \sim 6.57 \times 10^6$ which is 18 times more than in the multi-block case. This represents a saving of 18 times in the memory. Furthermore, since $\delta t = \delta x = \delta y$ in the LBE simulation, one time step in the coarsest grid system ($m = 8$) requires two time steps in the intermediate grid blocks and eight steps in the finest grid blocks. The ratio of the computational efforts required to carry out a single-block simulations to that for a multi-block simulation for a given period of physical time would be

$$6.57 \times 10^6 \times 8/(132\,225 \times 8 + 93\,200 \times 2 + 139\,628) \sim 38$$

Clearly, additional saving can be achieved if further blocks of different sizes are used. In a recent work [23], improvement of the efficiency and accuracy based on refined grid and variable time step is also demonstrated.

5. CONCLUDING REMARKS

A multi-block strategy is developed for the lattice Boltzmann method. The interface condition is derived to ensure the mass conservation and stress continuity between neighboring blocks. The present study demonstrates that the multi-block strategy can greatly improve the computational efficiency of the LBE method. Important computational issues, such as conservative

properties between grid blocks, accuracy assessment with respect to grid refinement, and the implications of corner singularities and the Reynolds number, have been addressed. With both accuracy and efficiency aspects improved, there is a significant potential for the multi-block strategy in the LBE method for practical flow problems.

ACKNOWLEDGEMENTS

The work reported in this paper has been partially supported by NASA Langley Research Center, with David Rudy as the project monitor. R. Mei also acknowledges partial support of the Engineering Research Center (ERC) for Particle Science & Technology at the University of Florida, the National Science Foundation (EEC-9402989), and Industrial partners of the ERC. The authors thank Dr Li-Shi Luo for many helpful discussions.

REFERENCES

1. McNamara G, Zanetti G. Use of the Boltzmann equation to simulate lattice-gas automata. *Physical Review Letters* 1988; **61**:2332–2335.
2. Higuera F, Succi S, Benzi R. Lattice gas dynamics with enhanced collisions. *Europhysics Letters* 1989; **9**:345–349.
3. Qian YH, d'Humieres, Lallemand P. Lattice BGK models for Navier–Stokes equation. *Europhysics Letters* 1992; **17**:479–484.
4. Benzi R, Succi S, Vergassola M. The lattice Boltzmann equation: Theory and applications. *Physics Report* 1992; **222**:145–197.
5. Chen S, Doolen GD. Lattice Boltzmann method for fluid flows. *Annual Review of Fluid Mechanics* 1998; **30**:329–364.
6. Peyret R, Taylor TD. *Computational Techniques for Fluid Dynamics*, vol. II. Springer-Verlag: New York, 1983.
7. Fletcher CAJ. *Computational Techniques for Fluid Dynamics*, vols. I & II. Springer-Verlag: New York, 1988.
8. Shyy W. *Computational Modeling for Fluid Flow and Interfacial Transport*, (corrected printing). Elsevier: Amsterdam, 1997.
9. Bhatnagar PL, Gross EP, Krook M. A model for collision processes in gases. I. Small amplitude processes in charged and neutral one-component system. *Physical Review* 1954; **94**:511–525.
10. He X, Luo L-S. A priori derivation of the lattice Boltzmann equation. *Physical Review E* 1997; **55**:R6333–R6336.
11. He X, Luo L-S. Theory of the lattice Boltzmann equation: From Boltzmann equation to lattice Boltzmann equation. *Physical Review E* 1997; **56**:6811–6817.
12. Mei R, Luo L, Shyy W. An accurate curved boundary treatment in the lattice Boltzmann method. *Journal of Computational Physics* 1999; **155**:307–330.
13. Shyy W, Udaykumar HS, Rao MM, Smith RW. *Computational Fluid Dynamics With Moving Boundaries*. Taylor & Francis: Oxford, 1996.
14. Ye T, Mittal R, Udaykumar HS, Shyy W. An accurate Cartesian grid method for viscous incompressible flows with complex immersed boundaries. *Journal of Computational Physics* 1999; **156**:209–240.
15. Filippova O, Hänel D. Grid refinement for lattice-BGK models. *Journal of Computational Physics* 1998; **147**:219–228.
16. Lin CL, Lai YG. Lattice Boltzmann method on composite grids. *Physical Review E* 2000; **62**(Part A):2219–2225.
17. Kandhai D, Soll W, Chen S, Hoekstra A, Sloot P. Finite-difference lattice-BGK methods on nested grids. *Computer Physics Communications* 2000; **129**:100–109.
18. Ghia U, Ghia KN, Shin CT, High-Re solution for incompressible flow using the Navier–Stokes equations and a mutigrid method. *Journal of Computational Physics* 1982; **48**:387–411.
19. Shyy W, Thakur SS, Ouyang H, Liu J, Blosch E. *Computational Techniques for Complex Transport Phenomena*. Cambridge University Press: New York, 1999.
20. Schäfer M, Turek S. Benchmark computations of laminar flow over a cylinder. *Notes in Numerical Fluid Mechanics*, vol. 52. Vieweg Verlag: Braunschweig, 1996; 547–566.
21. Drela M, Giles MB. Viscous-inviscid analysis of transonic and low Reynolds number airfoils. *AIAA Journal* 1987; **25**:1347–1355.
22. Lockard DP, Luo L-S, Singer BA. Evaluation of Powerflow for aerodynamic applications. Preprint, 2000.
23. Filippova O, Hänel D. Acceleration of lattice-BGK schemes with grid refinement. *Journal of Computational Physics* 2000; **165**:407–427.

